Tellus (1996), 48A, 424–441
Printed in UK – all rights reserved


TELLUS
ISSN 0280–6495

# Estimation of surface albedo from NOAA AVHRR data in high latitudes

By VESA LAINE* and MARTTI HEIKINHEIMO, *Finnish Meteorological Institute, P.O.B. 503, 00101 Helsinki, Finland*

(Manuscript received 22 May 1995; in final form 8 November 1995)

ABSTRACT

A method for determining the surface albedo from routine daily NOAA AVHRR data is described and tested for applicability under high latitude conditions in a boreal-sub-arctic region. The test period included all received satellite data from April to October 1994, giving a good coverage of various and changing surface conditions. Albedo values obtained initially for each cloud-free pixel and satellite over-pass were averaged over nine-day periods to include a full cycle of measuring geometries and to obtain an adequate number of cloud-free pixels in the final average images. With the automated image navigation provided by the present receiving system, spatial averaging over a minimum of 24 × 24 pixel squares was needed to obtain acceptable repeatability of local albedo values. The atmospheric correction was made using a bi-directional atmospheric correction method. In early April, the albedo over the sea in the ice-covered northern Gulf of Bothnia and in the open mountain regions was typically above 60%. Over snow-covered forested areas, the albedo was near 50% in the sub-arctic zone, and near 30% for the central boreal forest-covered surface. The difference in albedo between the northern and southern forested locations in the presence of snow was attributed to the higher biomass density of forests in the south and possibly more snow remaining on trees in the north. For snow-free conditions, forested areas typically showed an albedo in the range 11–13%. Agricultural regions, mixed with minor patches of forest, generally showed an albedo below 15% for conditions of low crop leaf area coverage, but reached as high as 18% under conditions of maximum leaf area coverage in mid-summer. Retrieval of the edge of snow cover in spring and the appearance of newly-fallen snow in autumn could readily be carried out using a threshold albedo of 20%.

## 1. Introduction

The rôle of surface albedo as a factor strongly affecting the earth's radiation balance has frequently been emphasised in studies of the global climate system. Snow and ice have generally a high reflectance, implying that regions having cold winter and relatively warm summer climates show strong seasonal variations in surface albedo. Realistic estimates of surface albedo at adequate spatial scales are a prerequisite for a realistic estimation of the global energy balance in atmospheric simulation models and for detecting changes in the radiation balance of the global climate system. Sensitivity studies with relatively simple energy balance models have for example shown that the atmospheric response to changes in the radiation balance is highly unstable; changes in the surface albedo have caused significant perturbations in the state of the atmosphere (Van der Veen, 1992). Long-term monitoring of the land surface albedo regionally in high latitudes as well as globally is best done using remote sensing from polar-orbiting satellites, of which the use of NOAA AVHRR is discussed here.

* Corresponding author.

Several factors complicate the determination of the surface albedo in practice. The available spectral bands used by the satellite represent only a fraction of the solar short-wave spectrum. The broadband albedo can be estimated using proportional constants for AVHRR channels 1 and 2 (Wydick et al. 1987; Di and Rundquist, 1994). Radiances at the earth's surface and at the satellite receiver are also affected by atmospheric scattering and absorption. The success of atmospheric correction algorithms therefore depends largely on the availability of information on the state of the atmosphere (Paltridge and Mitchell, 1990). To obtain the land surface albedo, cloud-free pixels need to be separated from pixels contaminated by radiances due to reflection from clouds. Methods for cloud detection can be divided into three categories: statistical methods based on the histogram analysis (Phulpin et al., 1983), pattern recognition methods based on the textural characteristics of the scene (Garand, 1988) and threshold methods (Allen et al., 1990; Derrien et al., 1993; Saunders and Kriebel, 1988) that are based on multispectral classification applied to the different spectral and thermal characteristics of surface types. More advanced methods can also be used to identify cloud type: automatic schemes for routine purposes have been reported by, e.g., Derrien et al. (1993), Liljas (1987) and by Karlsson (1989). Here a multispectral method based on AVHRR channels 1, 3 and 4 was used according to Allen et al. (1990).

Reflectance from land surface elements and from the atmosphere is non-isotropic i.e. the measured albedo depends on the relative positions of satellite and sun with respect to the surface point monitored. Particularly the bi-directional reflectance may distort albedo estimates over densely-vegetated areas (Paltridge and Mitchell, 1990) and over an aerosol-loaded atmosphere (Gerstl and Simmer, 1986). Taylor and Stowe (1984) have used data from the NIMBUS 7 Earth Radiation Budget Experiment (ERBE) to discover the properties of the bi-directional reflectance from earth and cloud surfaces and how these properties vary with solar angle. The measured albedo generally increased with increasing solar zenith angle, except with snow surfaces. Snow albedo showed very little variation with solar zenith angle. The same kind of results have been reported by Li and Garand (1994) and Suttles et al. (1988). Fast algorithms to correct for the visible and the near-infrared bi-directional reflectances of the ground from AVHRR data have been developed by Paltridge and Mitchell (1990) to alleviate the problem.

Recently Li and Garand (1994) developed a single equation that yields surface albedo under clear skies from the albedo at the top of the atmosphere as measured by the ERBE broadband sensor, the solar zenith angle and the total atmospheric precipitable water. The method was applicable for the estimation of both instantaneous and daily mean surface albedos at a spatial resolution of $2.5^\circ \times 2.5^\circ$ for the whole globe.

The present experiment demonstrates the methods potential applicability for estimating surface albedo in high latitudes, between ca. 55–70° N. Such continuous estimates can be used in long-term climate studies or operationally in weather prediction models such as HIRLAM. For these applications the image processing time and computer storage space may have to be limited by practical considerations, resulting in compromises in the resolution of albedo estimates in both time and in space. Adequate spatial resolution in this case is of the order of the grid size of a weather prediction model; i.e., areally-averaged estimates covering surface areas of about $25 \text{ km} \times 25 \text{ km}$ should satisfy all the present requirements of prediction models.

Significant temporal changes in surface albedo are much slower than the daily variation of weather conditions. For the detection of any relevant sub-seasonal changes of surface albedo, therefore, a weekly or bi-weekly time resolution should be about adequate. The relatively coarse time-resolution requirement allows the compositing of several sequential images with a consequent smoothing-out of unnecessary noise in the data, as will be explained below. The averaging of images is also required to fill in the unavoidable gaps in the data caused by cloudy areas or images of poor quality.

Satellite-based estimates of surface albedo were compared with previous measurements in the region made from aircraft with conventional broadband sensors (Solantie, 1988). The determination of the land surface cover and the presence of snow were based on digital geographical information and data from synoptic weather stations.

## 2. Theory

### 2.1. Definition of surface albedo

The broadband surface albedo $\alpha$ is defined as the ratio of the vertical components of the reflected radiation flux density to the incoming solar irradiance $F$. The following method was introduced by Paltridge and Mitchell (1990). For a Lambertian surface the atmosphere surface albedo $\alpha_i$ in channel i is given by

$$\alpha_i = \pi I_i^s / F_i \cos\theta_0 , \tag{1}$$

where $F_i$ = band-integrated solar flux density above the atmosphere, $\pi I_i^s$ = band-integrated reflected flux density, $\theta_0$ = solar zenith angle

NOAA calibrates the AVHRR channels in terms of a parameter $K_i$, called the "NOAA albedo" as

$$K_i = \pi I_i^s / F_i, \tag{2}$$

giving

$$\alpha_i = K_i / \cos\theta_0. \tag{3}$$

In reality, the atmosphere and ground surface are not Lambertian surfaces. Thus $K_i$ depends on the measuring geometry, i.e., $K_i$ is a function of the zenith and azimuth angles of both satellite and sun:

$$K_i = K_i(\theta_0, \theta_s, \Delta\psi), \tag{4}$$

where $\theta_0$ = solar zenith angle, $\theta_s$ = satellite zenith angle, $\Delta\psi$ = relative azimuth angle of satellite and sun.

### 2.2. Atmospheric correction

In the model presented by Paltridge and Mitchell (1990), the radiance $I^s$ received by the satellite was decomposed into the following components:

$$I^s = I^{\mathrm{dir}} + I^{\mathrm{sca}} + I^{\mathrm{sky}} + I^{\mathrm{ind}} + I^{\mathrm{mul}} , \tag{5}$$

where $I^{\mathrm{dir}}$ = radiation directly reflected by the ground, $I^{\mathrm{sca}}$ = radiation singly scattered by molecules and particles in the atmosphere, $I^{\mathrm{sky}}$ = radiation singly scattered into a diffuse flux which impinges on the ground and is reflected directly to the satellite, $I^{\mathrm{ind}}$ = radiation reflected by the ground and subsequently scattered to the satellite, $I^{\mathrm{mul}}$ = multiply scattered radiation by molecules and particles.

Following Paltridge and Mitchell, the parametrizations for $I^s$ for computational use, valid for the wavelength range of channels 1 and 2 were as follows:

$$(1-M)I^s = (1-M)KF/\pi = 4R\cos\theta_0\, g(m)\mathrm{e}^{-mt} \times (1+m\tau) + \sec\theta_s \sum_{j=0}^{1} \Phi_j Q_j(m), \tag{6}$$

where $M$ = fraction of $I^s$ contributed by molecular multiple scattering, $R$ = surface bidirectional reflectance, $m$ = total sun-target-sensor air mass = $\sec\theta_0 + \sec\theta_s$, $\tau$ = aerosol vertical optical depth, $\theta_s$ = solar zenith angle, $\Phi_0$ = molecular scattering phase function = 0.75 $(1+\cos^2\Theta)$, $\Phi_1$ = aerosol scattering phase function = $4\pi\exp(11.3\mathrm{e}^{-0.018\Theta} + 0.032\Theta - 9.2)$, $\Theta$ = scattering angle, $Q_0(m)$ = integrated molecular scattering source function, $Q_1(m)$ = integrated aerosol scattering source function, $g(m) = a_1 \exp(-b_1\, m)$, $Q_0(m) = a_2\exp(-b_2\, m)$, $Q_1(m) = (1-\mathrm{e}^{-m\tau})g(m)/m$.

The values of $\tau$, $M$, $g(m)$, $Q_0(m)$ and $Q_1(m)$ for AVHRR channels 1 and 2 were calculated using the values of the constants given in Table 1.

By modifying eq. (6) and normalizing the solar flux density $F$ to $\pi$, the surface directional reflectance $R$ for channels 1 and 2 may be written (Paltridge and Mitchell, 1990):

$$R(\theta_s, \theta_0, \Delta\psi) = \frac{K(1-M) - \sec\theta_s \sum_{j=0}^{1} \Phi_j Q_j(m)}{4\cos\theta_0\, g(m)\mathrm{e}^{-m\tau}(1+m\tau)} . \tag{7}$$

The broadband albedo $\alpha$ can then be calculated using a simple regression equation (He et al., 1987), cited in (Di and Rundquist, 1994):

$$\alpha = 0.322\, R_1 + 0.678\, R_2 , \tag{8}$$

where $R_1$ and $R_2$ are the reflectances calculated from eq. 7 for AVHRR channels 1 and 2 respectively.

Table 1. *Values of constants $a_1$, $b_1$, $a_2$, $b_2$, $M$ and $\tau$ used in eq. 6 (after Paltridge and Mitchell, 1990)*

| Quantity | Channel 1 | Channel 2 |
|---|---|---|
| $a_1$ | 0.2500 | 0.2350 |
| $b_1$ | 0.0853 | 0.0724 |
| $a_2$ | 0.0145 | 0.0049 |
| $b_2$ | 0.0441 | 0.0335 |
| $M$ | 0.10 | 0.05 |
| $\tau$ | 0.10 | 0.07 |

*2.3. Sensitivity to measuring geometry, aerosol optical depth and precipitable water*

Tests were made to discover the amount of atmospheric correction i.e. the difference between the albedo at the top of the atmosphere and surface albedo. The assumed TOA albedos were fixed at 10%, 30% and 50%, and the assumed range of the solar zenith angle $\theta_0$ was from 40° to 70°.

The Paltridge and Mitchell atmospheric correction scheme (eq. (7)) takes into account explicitly the effect of the relative positions of satellite and sun with respect to the surface target point, and the atmospheric transparency for aerosols. Implicit in this scheme is the assumption of constant precipitable water (1.44 cm), in contrast with the scheme introduced by Li and Garand (1994). The relationship between TOA albedos and the NOAA albedos $K$ for eq. (7) was calculated using eq. (3). The values of $K$ corresponding to the assumed TOA albedos were then substituted in eq. (7). The calculations for Figs. 1a and 1b were made using eqs. (7) and (8).

For Fig. 1a, an investigation was made into the effect of satellite zenith angles of 40°, 0° and −40° on the computed values of the surface albedo. The aerosol optical depths were taken as $\tau_1 = 0.1$ and $\tau_2 = 0.07$ as appropriate at the wavelengths of channels 1 and 2. (The 40° and −40° satellite zenith angles corresponded to 0° and 180° relative azimuth angles, respectively, of satellite and sun.) For Fig. 1b the effect of aerosol optical depths of $\tau_1 = 0.1$, 0.2 and 0.3 (where $\tau_2 = 0.7 \times \tau_1$) on the surface albedo was tested at a fixed satellite zenith angle of 0°.

The dependence of the surface albedo estimates on the atmospheric precipitable water was tested using the scheme of Li and Garand (Fig 1c). The method is based on broad-band Earth Radiation Budget Experiment (ERBE) reflectance observations with in-flight calibration and bidirectional corrections. The use of a broad-band sensor removes the uncertainty in the estimation of the broad-band albedo from narrow-band satellite measurements. The input parameters for the following parameterization are the TOA albedo, the solar zenith angle and the precipitable water.

$$\alpha_s = a(\mu, p) + b(\mu, p)\alpha_t , \qquad (9)$$

where $\alpha_s$ = surface albedo, $\alpha_t$ = TOA albedo, $\mu$ = cosine of solar zenith angle, $p$ = precipitable water (cm), $a(\mu, p) = a_1(p) + a_2(p)1/\mu$, $b(\mu, p) = b_1(p) + b_2(p)1/\mu$; and $a_1(p) = -0.96882 + 0.71800\sqrt{p}$, $a_2(p) = -4.11460 - 0.76347\sqrt{p}$, $b_1(p) = 1.16711 + 0.05963\sqrt{p}$, $b_2(p) = 0.07514 + 0.04105\sqrt{p}$.

In the scheme of Li and Garand the aerosol optical depth was fixed as 0.05 at 0.55 μm. Results for values of precipitable water of 1.0, 2.0 and 3.0 cm are shown in Fig. 1c.

The results of the sensitivity analysis were as follows. In Fig. 1a, the surface albedo at levels of 30% and 50% was greater than the TOA albedo for all the zenith angles of both satellite and sun, being highest for the satellite's zenith angle of −40° and lowest for 40°. At a level of 10% the surface albedo was about the same as the TOA albedo for a satellite zenith angle of 0°, and smaller for satellite zenith angles of 40° and −40°. The difference between the TOA albedo and the surface albedo increased with increasing solar zenith angle. The influence of satellite zenith angle and the relative azimuth angle on the computed surface albedo was about 2% (absolute units) at all the albedo levels, regardless of the solar zenith angle. Such being the case, the influence of satellite zenith angle on the computed surface albedo was much smaller than the influence of solar elevation, at least for low values of aerosol optical depth.

Fig. 1b shows the dependence of surface albedo on aerosol optical depth. The differences between the surface albedo and the TOA albedo at levels of 30% and 50% increased further with increasing aerosol optical depth. This was especially notable for greater values of solar zenith angle. At high albedo levels (50–60%) and high values of solar zenith angles (60–70°) an increase in aerosol optical depth from 0.1 to 0.3 caused an increase of 8–10% (absolute units) in computed surface albedo, whereas at lower albedo levels (10%) the influence of aerosol was insignificant. Thus, for example over snow-covered surfaces and when the sun is low, a heavy aerosol loading may cause a significant underestimation of the surface albedo if the aerosol optical depth is not known. Overestimations can occur in the case of very small surface albedos, such as over water surfaces, where most of the received radiation can come from aerosol scattering.

In Fig. 1c, the difference between the surface albedo and the TOA albedo at levels of 30% and 50% were analogous to Figs. 1a, b; however, the

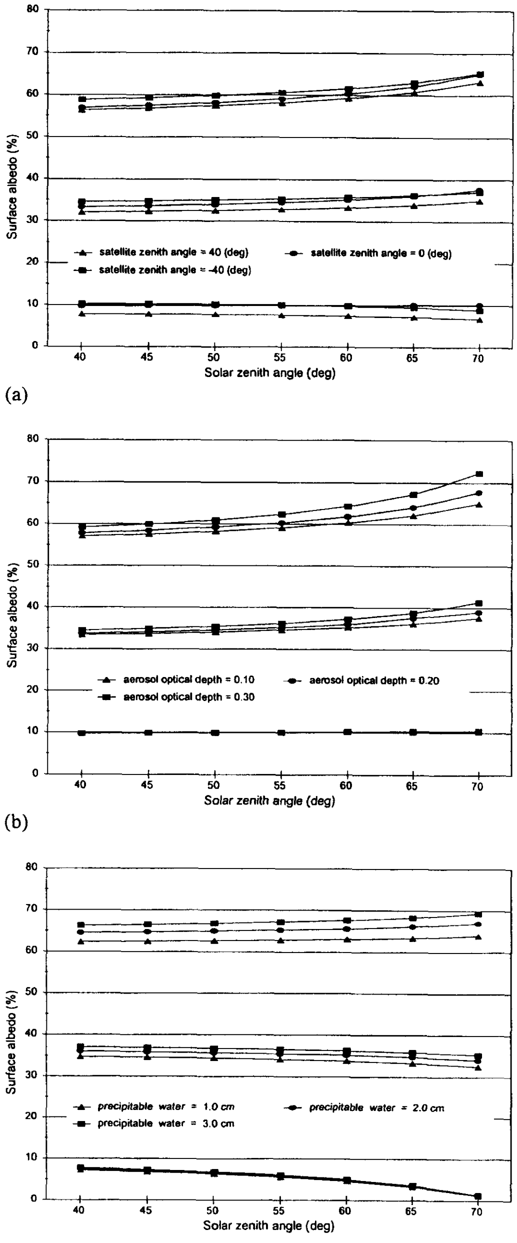


Fig. 1. The dependence of the calculated surface albedo upon (a) solar zenith angle at satellite zenith angles of 40°, 0° and −40° and with an aerosol optical depth of $\tau_1 = 0.1$, (b) solar zenith angle with aerosol optical depths of $\tau_1 = 0.1$, 0.2 and 0.3 and with a satellite zenith angle of 0°, (c) solar zenith angle with precipitable water of 1.0, 2.0 and 3.0 cm and with an aerosol optical depth of 0.1 at 0.55 $\mu$m. The dependencies were calculated for three assumed TOA albedos: 10, 30 and 50%.

decrease of the surface albedo at 10% level was notably stronger than in Figs. 1a, b. The effect of the precipitable water on the calculated surface albedo was insignificant at an albedo level of 10%. At a level of 30% the increase in precipitable water from 1.0 to 3.0 cm caused an increase of about 4% (absolute units) in the computed surface albedo, while at a level of 50% the increase in surface albedo was about 7%. Thus, under conditions of higher surface albedos, lack of information about the atmospheric precipitable water may be a significant source of error when estimating the surface albedo.

The results of both schemes agreed with reality in the sense that with high surface albedos the major part of the reflected radiation received by the satellite comes from the surface with only a minor contribution from the atmosphere. In this case the atmosphere attenuates the received radiation, so the surface albedo is higher than the TOA albedo. In the case of small surface albedos such as water surfaces, most of the received radiation comes from atmospheric scattering. The TOA albedo must then be higher than the surface albedo.

On the basis of the sensitivity test use was made in this study of eqs. (7) and (8) with an assumed satellite zenith angle of 20° and a relative azimuth angle of satellite and sun of 180°. The assumed values of aerosol optical depths for channels 1 and 2 were 0.10 and 0.07 (after Paltridge and Mitchell), respectively. Operational data of aerosol optical depth in high latitudes were not available. For estimating the surface albedo over vegetated surfaces the missing information regarding the exact measuring geometry, the aerosol optical depth and the precipitable water can only cause an error of about 0–2%. In theory, over snow-covered surfaces the error at its maximum may even be 10–15%. However, in Finland average values of precipitable water in April and May, when snow and ice are present, are 1.0–1.4 cm (calculated from Climatological Statistics in Finland 1961–1990, Finnish Met. Institute). On the assumption that the values are less than or equal to the constant value in Paltridge and Mitchell scheme (1.44 cm) the error due to precipitable water may be considered negligible. The only significant source of error using this scheme is then the variability of aerosol optical depth.

## 3. Material

### 3.1. *Data preprocessing*

A data processing system, known as FIMSAT and developed by the Technical Research Centre of Finland in 1987, was used for receiving and preprocessing satellite images at the Finnish Meteorological Institute (FMI). Only daytime AVHRR data from the NOAA-11 and NOAA-12 polar-orbiting satellites was used for this experiment. The orbiting period was approximately 100 min, the average height of the orbit being at about 850 km above the earth's surface. The satellites produced images from five different AVHRR (advanced very-high-resolution radiometer) channels, of which channel 1 is situated in the range of visible light wavelengths (0.58–0.68 $\mu$m), channel 2 is in the near-infrared (0.72–1.10 $\mu$m) and channel 3 is in the mid-infrared region (3.55–3.93 $\mu$m). Channel 4 (10.3–11.3 $\mu$m) and channel 5 (11.5–12.5 $\mu$m) are situated in the far-infrared region. The NOAA 11 and NOAA 12 calibration gain coefficients for channels 1 and 2 are presented in Table 2 (Teillet and Holben, 1994). The values for postlaunch day 0 were available in the FIMSAT receiving system, and were used here.

On the basis of Table 2, the sensitivity of NOAA 11 visible and near-infrared instruments in practice has remained stable and therefore has no significant effect on the surface albedo calculations. For NOAA 12, later calibration coefficients were not available.

The images produced by the receiving system were denoted as standard images, whose image area, resolution, spectral channels and channel scaling were chosen. The standard image was resampled into the stereographic geographical projection using the received track parameters. This geometrical correction was computed in advance of the actual overflight on the basis of a received telex message containing the values of the satellite's orbital parameters. The present system, however, did not provide as output of the satellite's zenith and azimuth angles. A quality factor $Q$ contained in this message could be used for estimating how near to the receiver antenna the overflight would occur. FIMSAT also compressed the original ten-bit raw data into eight-bit resolution with the digits from 0 to 239 used for scaling the radiance data and those from 240 to 255 for a file description. For the visible and near-infrared channels (channels 1 and 2) the transformation from raw values to values of albedo was made using a linear scale with the help of satellite-specific parameters supplied by NOAA. For the calibration of the far-infrared, i.e., the heat channels 3, 4 and 5, the radiances were directly converted into target temperatures. This calibration was based upon temperature and emission measurements of the satellite's internal calibration sources as well as the emission from space (source: FIMSAT, Users' Manual, Technical Research Centre of Finland, 1987).

### 3.2. *Spatial resolution*

Due to inaccuracies in the received telex of orbital parameters and in the navigation software

Table 2. *Calibration gain coefficients for the NOAA 11 and NOAA 12 AVHRR instruments (Teillet and Holben, 1994) (*Teillet, personal communication, 1995)*

| Satellite | Postlaunch day | Gain ch. 1 | Gain ch. 2 |
|---|---|---|---|
| NOAA 11 | 1988–09–24 (0) | 1.70 | 2.61 |
| | 1989-Feb (157) | 1.67 | 2.47 |
| | 1989-Aug (341) | 1.68 | 2.42 |
| | 1990-Feb (522) | 1.65 | 2.38 |
| | 1990-Aug (706) | 1.70 | 2.44 |
| | 1991-Feb (887) | 1.69 | 2.43 |
| | 1991-Aug (1071) | 1.69 | 2.45 |
| | 1992-Aug (1437) | 1.69 | 2.45 |
| | 1993-Dec (1925)* | 1.71 | 2.44 |
| | 1994-Dec (2290)* | 1.69 | 2.40 |
| NOAA 12 | 1991–05–14 (0) | 1.87 | 2.95 |

the consequent images routinely produced by FIMSAT fell slightly short of a perfect geographical overlap. The magnitude of the geographical shift was analysed by selecting 29 overflights exhibiting near clear-sky conditions in July 1994. The x- and y-coordinates (in the image's arbitrary coordinate system) of six easily identifiable geographical control points in the satellite image (see Fig. 2) were determined manually to an accuracy of 2 pixels. The statistics of the shifts at the control points are summarized in Table 3. Based on these results the average mismatch between consecutive images was about 5 pixels, corresponding to a displacement of about 6 km.

### 3.3. *Detection of clouds*

The reflectance values of different surfaces were used to separate land and snow from clouds. The threshold method allows fast and simple cloud detection computations in an automatic surface albedo model.

Typical observed reflectances for NOAA-9 AVHRR channel 1 and channel 3 over land, snow


*Fig. 2.* The grid network based on 24 × 24 pixel squares and the location of the selected test squares representing land surface types. The control points for testing the accuracy of the relative positioning of sequential images are numbered from 1 to 6.

Table 3. *Control points, standard deviations (STD) and the number of cloud-free occasions (N)*

| Control point | STD (x) | STD (y) | N |
|---|---|---|---|
| 1 Pyhäjärvi | 4.8 | 4.2 | 19 |
| 2 Ristna | 6.2 | 4.8 | 26 |
| 3 Suursaari | 6.4 | 3.9 | 15 |
| 4 Kotlin | 7.4 | 3.7 | 17 |
| 5 Valamo | 6.3 | 3.6 | 17 |
| 6 Oulujärvi | 4.7 | 3.6 | 12 |
| 1–6 | $\text{mean}_{STD(x)} = 6.0$ | $\text{mean}_{STD(y)} = 4.0$ | $N_{tot} = 106$ |

Table 4. *Summary of NOAA-9 AVHRR observed channel 1 reflectance ($R_1$) and channel 3 reflectance ($R_3$) for 900 land pixels, 1600 ice cloud pixels, 1300 liquid cloud pixels and 1000 snow pixels (Allen et al. 1990)*

| Surface | ($R_1$) | ($R_3$) |
|---|---|---|
| Liquid cloud | 0.38–0.77 | 0.08–0.36 |
| Ice cloud | 0.15–0.86 | 0.02–0.27 |
| Land | 0.09–0.18 | 0.03–0.10 |
| Snow | 0.48–0.84 | 0.02–0.04 |

and clouds is presented in Table 4, based on data by Allen et al. (1990).

Daytime channel 3 radiance consists of both solar reflection and thermal emission. Following Allen et al. (1990) the measured radiance for channel 3 is presented as follows:

$$I_3 = \varepsilon_3 B_3(T) + R_3(\theta_0, \theta_s, \Delta\psi) I_0 \cos\theta_0 , \qquad (10)$$

where $\varepsilon_3 B_3(T)$ = channel 3 thermal emission of the surface, $R_3(\theta_0, \theta_s, \Delta\psi)$ = channel 3 reflectance, $I_0 \cos\theta_0$ = cosine-weighted incident solar radiance.

Assuming here a Lambertian surface and $\varepsilon_3 B_3(T) \approx \varepsilon_4 B_4(T)$ (channel 4 thermal emission of the surface), a simplified representation for channel 3 reflectance can be estimated by subtracting the channel 4 brightness temperature from the measured channel 3 brightness temperature (see Liljas, 1987). A reflectance threshold of $R_3 = 0.10$ was used for the separating of clouds from snow and land. In addition in summer time after melting of snow the reflectance of channel 1 with a threshold of $R_1 = 0.40$ was used. The values of $R_1$ and $R_3$ greater than the thresholds were assumed to be due to clouds. In spring and late autumn the cloud detection method based on $R_3$ was somewhat erroneous in those cases in which ice clouds occurred over snow- or ice-covered surfaces. By visual checking of the efficiency for the separation between snow and clouds, over approx. 95% of the pixels contaminated by clouds could be detected when snow or ice were present and nearly 100% under snow-free conditions.

### 3.4. *Averaging of images*

The final spatial scale of the albedo images was largely dependent on the relative positioning accuracy of individual images, determined to be on average 6 km or about 5 pixels. As a result the albedos initially calculated for each pixel were averaged spatially to minimize noise caused by the positioning error. In practice spatial averaging was made within squares of $24 \times 24$ pixels giving a spatial scale of 700 km$^2$ at the satellite nadir.

An averaging procedure was further designed to obtain wide geographical coverage of surface albedo from a series of single images each containing only patches of cloud-free areas. The averaging of information in time was also done to avoid systematic bias caused by varying satellite-target-sun geometry. An averaging period of nine days was chosen in order to cover a full cycle of measuring geometries for the final average image in accordance with Gutman (1988). The period of nine days was long enough to accumulate a selection of good quality images and maximize coverage of cloud-free pixels, while on the other hand the period was not too long to hinder the detection of typical seasonal changes in the surface albedo.

For the present experiment the average albedo images covered a region of North-Eastern Europe having its south-west corner located at 59.05° N, 17.33° E and north-east corner at 67.11° N, 49.95° E. The image area was divided into $40 \times 52$ grid squares with $24 \times 24$ pixels in each square, Fig. 2. The squares were numbered from 0 to 2079.

A few grid squares representing different dominating surface types, i.e., open sea water, coniferous forest, lakes mixed with forests, bogs and agricultural fields were selected for further analysis of the regional albedo values obtained. The locations of the test squares are also shown in Fig. 2. The relative accuracy of the method was evaluated by examining the variation of consecutive estimates of surface albedo and determining the distributions of the albedos of individual pixels within the test squares. The mean albedo was calculated by averaging all cloud-free pixels in the test square. In addition the maximum and minimum, the standard deviation and the fraction of the cloud-free pixels within the test squares were determined.

Averaged albedo images were calculated for consecutive 9-day periods from April to October 1994. The spatial variation was visualized as contour plots. The albedo distributions in spring and in late autumn were compared with the spatial analyses of snow depth over Finland obtained from surface measurements carried out by FMI. The albedo values obtained from satellite remote sensing were also compared with the typical albedo values for different land types in Finland obtained from aircraft observations (Solantie, 1988).

## 4. Analysis of albedo data

### *4.1. Seasonal variation of albedo over different surface types*

The locations of the 700 km$^2$ test squares numbered according to their sequence in the grid as 330, 779, 1126 and 1528, and representing respectively the dominant surface types of forests, lakes, sea water and agricultural fields are shown in Fig. 2. The distribution of surface type over land areas was determined according to digital land survey information available from the Environment Data Centre, National Board of Hydrology in Finland. This land survey information, based on LANDSAT images combined with ground verification, was organised digitally as percentages of the main land cover types (originally determined for $25 \times 25$ m squares) within $10 \times 10$ km rectangular grids. An example of the distribution of open land cover types, for agricultural fields, open bogs and high moorland, having typically a relatively high surface albedo, is shown in Fig. 3.

A further breakdown into percentage distributions of land surface types within each test square, based on digital land survey information is given in Table 5.

The objective in the selection of test squares was to perform quality assurange tests on the albedo data obtained with the present acquisition system. Specifically, we looked at the variation of the albedo from early spring to late summer for each square and the distribution of the albedo within each square, based on pixel data.

The seasonal variation of surface albedo for the test squares from April to October 1994 for consecutive nine-day averaged images is shown in Fig. 4, in which the Julian day on the date-axis denotes the middle of each 9-day period. In early April the highest albedo, 65%, was found over the ice-covered sea (square no.1126) in the northern Gulf of Bothnia. Over land areas, the albedo for square no. 1528, designated as forest and located near the northern limit of the Boreal forest zone, exhibited an albedo of 50% as compared to 30% for the forest/lake square (no. 779) further south in eastern Finland. The difference in albedo between these northerly and more southerly locations may be explained by probably more snow remaining on the forest canopy and an overall lower density of forest in northern Finland as compared to the more southerly forest/lake square. The albedo difference between squares 1528 and 779 may also be caused by the properties of the snow; i.e. the reflectance of wet melting snow in square 779 is lower than the reflectance of dry frozen snow in square 1528. In April, agricultural fields were mostly snow-free in south-western Finland, resulting in a relatively low albedo of near 13%

Table 5. *Proportional (in %) distributions of land types inside the squares; square numbers refer to Fig. 2*

| square no. | 330 | 375 | 779 | 1135 | 1528 |
|---|---|---|---|---|---|
| lakes | 0.2 | 1.1 | 17.8 | 2.5 | 2.3 |
| fields | 45.9 | 44.3 | 8.6 | 4.0 | 1.4 |
| forest | 43.5 | 37.7 | 58.2 | 61.1 | 56.8 |
| bogs | 2.0 | 1.7 | 6.0 | 16.1 | 13.1 |
| open bogs | 0.1 | 0.1 | 0.5 | 0.9 | 7.3 |
| forest clearing | 4.0 | 7.8 | 7.8 | 15.0 | 12.5 |

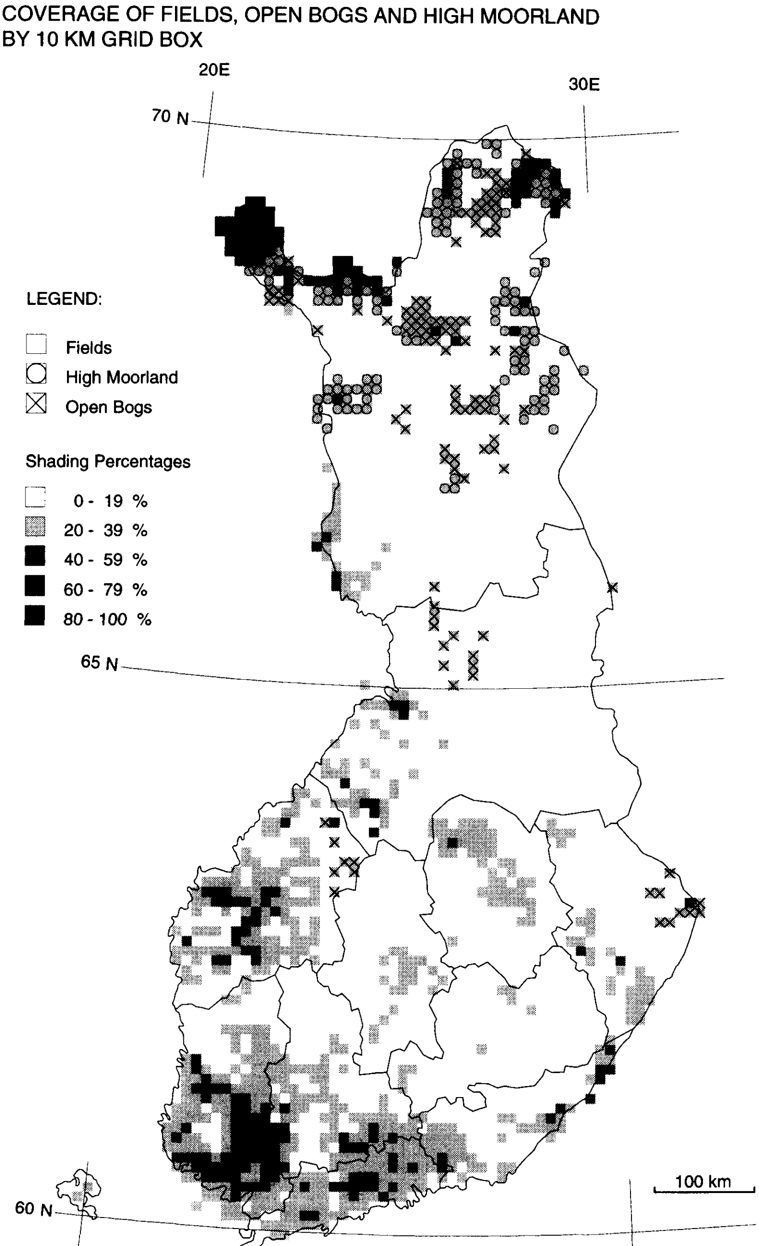


*Fig. 3.* Coverage of fields, high moorland and open bogs as a percentage of the $10 \times 10$ km grid surface area in Finland, based on land surface classification (source: Environmental Data Centre, National Board of Hydrology, Finland).

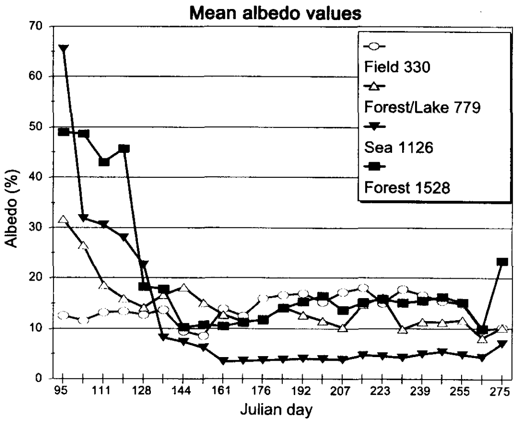


*Fig. 4.* The annual variation of the surface albedo from April to October in 1994, based on the test squares of averaged AVHRR images.

for square no. 330, with a high contribution from open agricultural areas.

Comparison of albedos between test squares from May onwards, under conditions free of snow and ice, revealed some features of the system performance and sensitivity to vegetation growth and surface moisture. The albedo over the sea (square no. 1135) settled down to about 5%, remaining constant through the summer season. The aircraft observations by Solantie (1988) for which the sea albedo had a value in of 5% (clear sky) support this value obtained for open water. In addition, for this test square, the variation of albedo in time between consecutive estimates was relatively small. This leads to the conclusion that the noise, particularly that caused by undetected cloudy pixels, was likely to be small for most of the period studied. Over heterogeneous land surfaces some noise was expected due to the imperfect overlap of sequential images used to form an albedo map. On the other hand, variation of the surface albedo over land areas was also expected due to natural causes, e.g. due to an increase in leaf area density and the occurrence of dry and moist periods during the course of the warm season. A close comparison of nine-day precipitation totals estimated for the test squares from station data and the average albedo values, Fig. 5, suggested a small but definite negative correlation between the two variables, particularly for the squares with an abundance of agricultural land. Also the observed average increase of albedo during summer time for the squares located in southern Finland corresponded to the expected gradual growth of leaf area density until mid-July followed by the yellowing of agricultural crops towards late August.

### 4.2. *Variation of albedo within test squares*

The within-square variation of albedo was studied by storing albedo values of individual cloud-free pixels for the nine-day-long sampling period. The resulting frequency distributions of surface albedo obtained for test squares 330, 779, 1126 and 1528 are shown in Fig. 6 for a case in spring (9–17 April) and in the middle of summer (7–15 July). Also shown in Fig. 6 are the basic statistics of surface albedo variation obtained for each test square and the proportion of cloud-free pixels.

In April the the surface albedo for open sea (square no. 1126) varied from 5% to 59%, due to the presence of both open water and sea ice. During summer the distribution of the albedo within this square was highly peaked around 5% as expected. For the northern forest square (no. 1528) in April the average albedo was near 50%, with a range of variation from 28% to 65% due to presence of snow. By comparison, in the mid-summer case, for the same square, a range of variation of only about $\pm 3\%$ around the average 15% was obtained. Distributions obtained for the square containing an abundance of agricultural fields (square no. 330) were rather well-established; in April a range of values from 8% to 21% was obtained, indicating the presence of both snow-free bare soil and coniferous forest; for the summer case, albedo values peaked near 17% and were well-explained by the presence of a mixed forest and green cultivated surface during conditions of maximum leaf area.

### 4.3. *Regional variation of surface albedo*

In Fig. 7, the regional variation of surface albedo in July estimated from two sources is compared. In Fig. 7a is shown the analysis for July 1994 representing the present experiment with the monthly-averaged AVHRR image computed using the algorithms described above. To explain some of the variation, the albedo map can be compared with the digitised information on land cover in

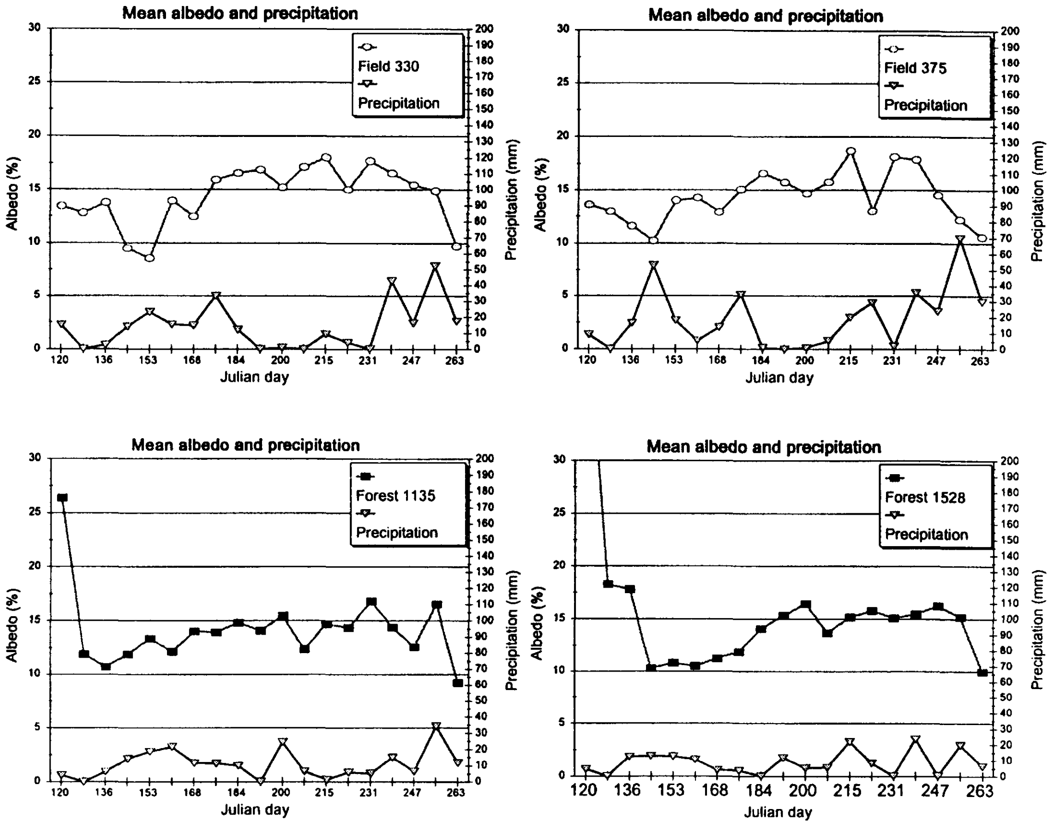


*Fig. 5.* The effect of ground humidity (amount of precipitation) on the surface albedo in the field and forestry land test squares of averaged AVHRR images during the snow-free period of 1994.

Fig. 3, showing a dominance of agricultural fields, open bogs and high moorland. The surface albedo for these regions characterised by relatively open terrain was typically between 15% and 18% during mid-summer. Over land regions mostly covered by coniferous forests in Central and Eastern Finland, the average albedo exhibited typically lower values, i.e. from 11% to 13%. The albedo for regions in the north where open bogs or high moorland dominated range from 14% to 18%. Previously, more detailed measurements on land surface albedo by Solantie (1988) were made from low-flying aircraft during summer conditions. These measurements provided a valuable source for comparison. The following summer-time surface albedos for the corresponding region and various surface types were reported: agricultural fields in July 20%, coniferous forest 11%, open bogs 17% and open sea 5% (clear sky). Surface albedos obtained in the present study were close to those obtained by Solantie (1988), showing perhaps a somewhat smaller range of variability between land surface types. This result is, nevertheless, expected since the spatial resolution available in the present system did not allow the distinguishing of homogenous patches such as those measured from a few hundred metres above the ground with airborne sensors.

In Fig. 7b is presented the spatial analysis of the climatological surface albedo for the corresponding calendar date in summer 1995 as derived recently for use as input to the HIRLAM model. The climatological albedo was based on several global and local data sets of fractions of land surface types and land/water distributions (Bringfelt et al., 1995). The classification for albedo estimates separated three basic surface types: forests, open land (fields, marshes, bogs, etc.) and

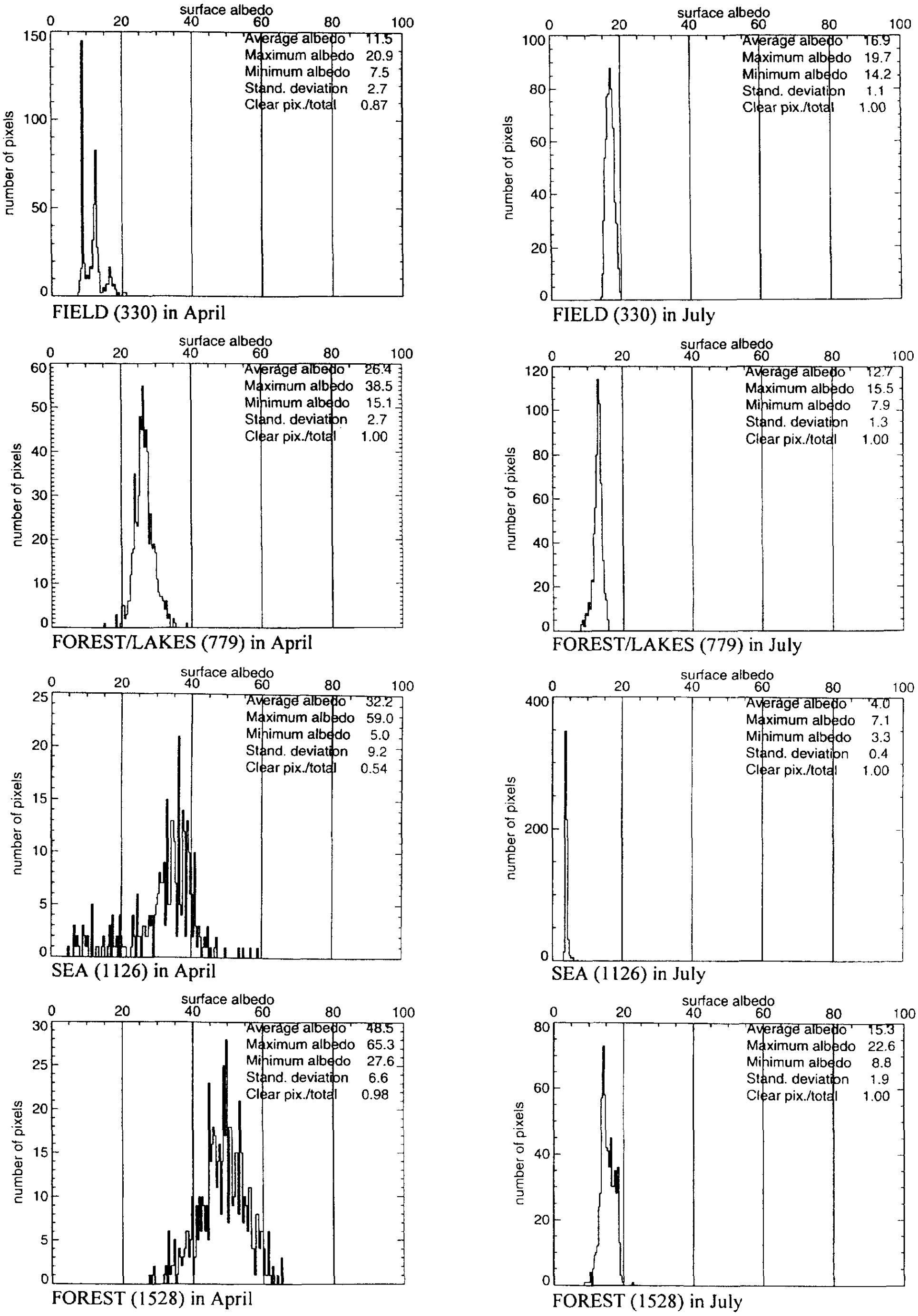


*Fig. 6.* Distributions of surface albedo after cloud removal within the selected test squares (330, 779, 1126, 1528) in April (left) and in July (right) in 1994, computed from the averaged images.

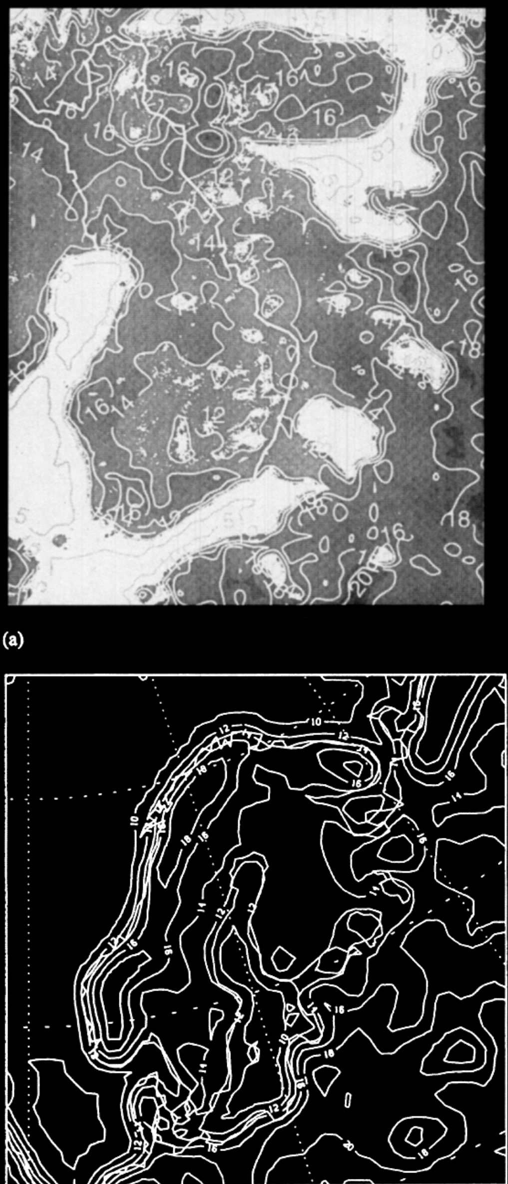

(a)

(b)

*Fig. 7.* Comparison of surface albedo distributions in Northern Europe representative of typical mid-summer conditions obtained with two independent methods: (a) the estimate based on near real-time (7–15 July 1994) remote sensing from NOAA AVHRR, and the method described in the text, and (b) the estimate presently used in the HIRLAM model. The latter estimate was based on typical values of albedo for water, forest and open land weighted in each grid square by the areal fractions of the three surface classes (Bringfeldt et al. 1995).

water (sea and lakes). Prescribed albedo values were assigned to each of these classes by assuming some values for albedos given in literature, allowing also for some seasonal variation in albedo based on information in literature sources. The albedo values used in the HIRLAM model were 0.07 for water, 0.10 for forest and 0.20 for open land. Despite the fact that the analyses produced by the two methods represented different years, the comparison should be justified for the summertime cases shown here.

Overall, the patterns of albedo variation are very similar in both sets of analyses, despite the fact that more spatial detail is shown in the AVHRR-based albedos due to the coarser resolution (55 km × 55 km) of the routinely-used HIRLAM version. A closer comparison shows that the AVHRR based albedo values are in general 2–4% (absolute units) higher, especially over open land areas (see Fig. 3 for land surface classification). On the other hand, for open sea, the climatological albedo estimate is about 3–5% higher than the present AVHRR-based estimate. The comparison demonstrates that the present AVHRR based estimates of surface albedo are in general comparable with the corresponding climatological estimates based on land-surface classification. On the other hand, if a reduced grid resolution is used for weather prediction, as in some test runs of the model, the present AVHRR-based analyses of surface albedo could even supercede the more conservative climatological values, particularly over ice-covered oceans and in regions where weather observation networks are sparse.

To demonstrate the sensitivity of the measured surface albedo to the existence of snow, a set of albedo distributions from April to June and for a case in October 1994 are presented in Fig. 8 (a–i). The changes in albedo during the spring period were mainly caused by the withdrawal northwards of the snow line. For verification, concurrent analyses of snow depth, based on station data over Finland are presented in Fig. 9 (a–i). Based on these data, the threshold albedo indicating the presence of snow or ice was near 20%. The albedo of snow above this threshold can vary within a wide range, depending on the properties of the snow cover; particularly for fresh snow the albedo is expected to be above 70%. With the spatial resolution of 700 km$^2$ used in the present study,

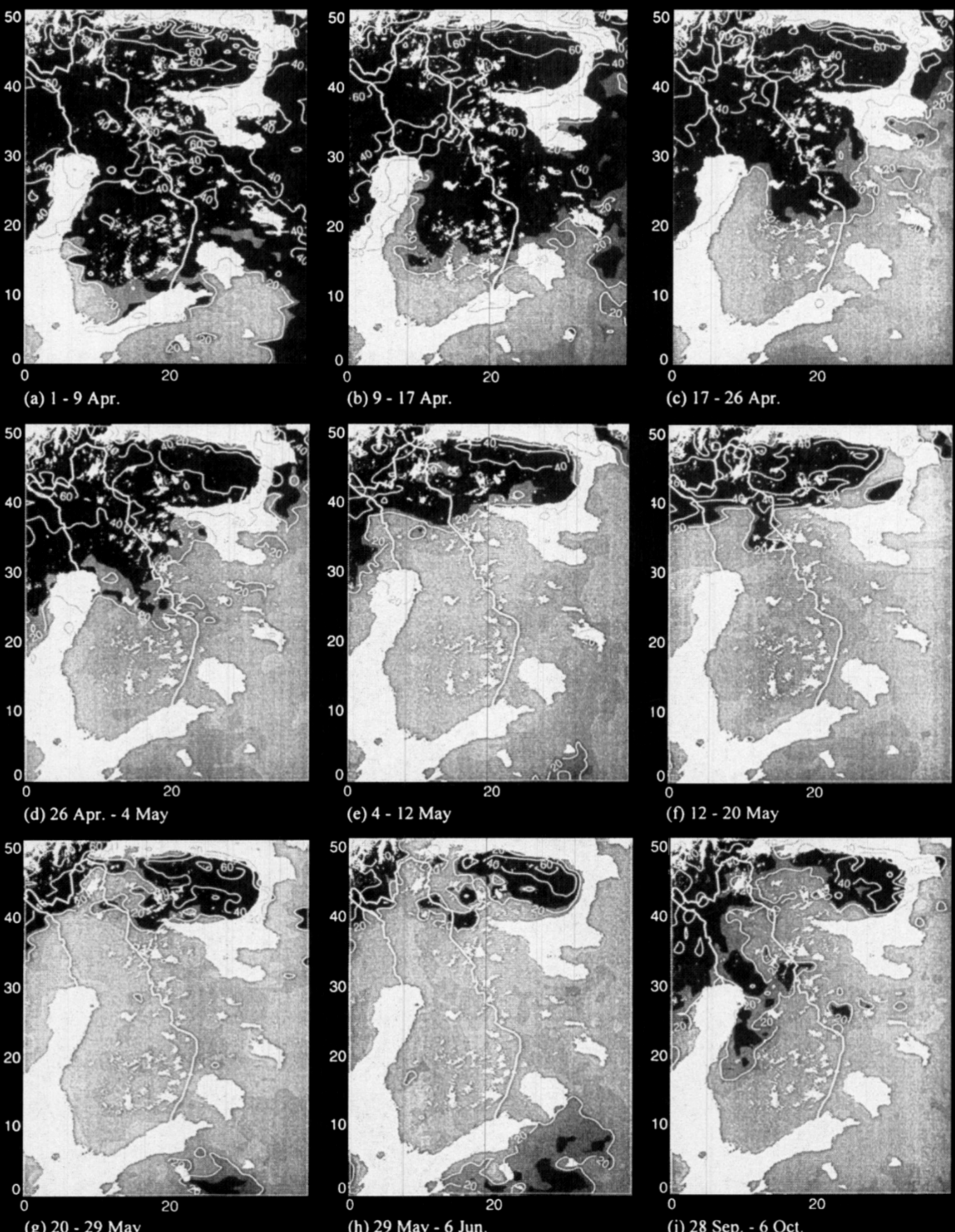


*Fig. 8.* Averaged surface albedo images from AVHRR data from April to June in 1994 (a–h), and a selected case from autumn after the first snowfalls in September/October (i). Regions in the north shown in white indicate albedo values above 20 %, which are usually found in the presence of snow cover.

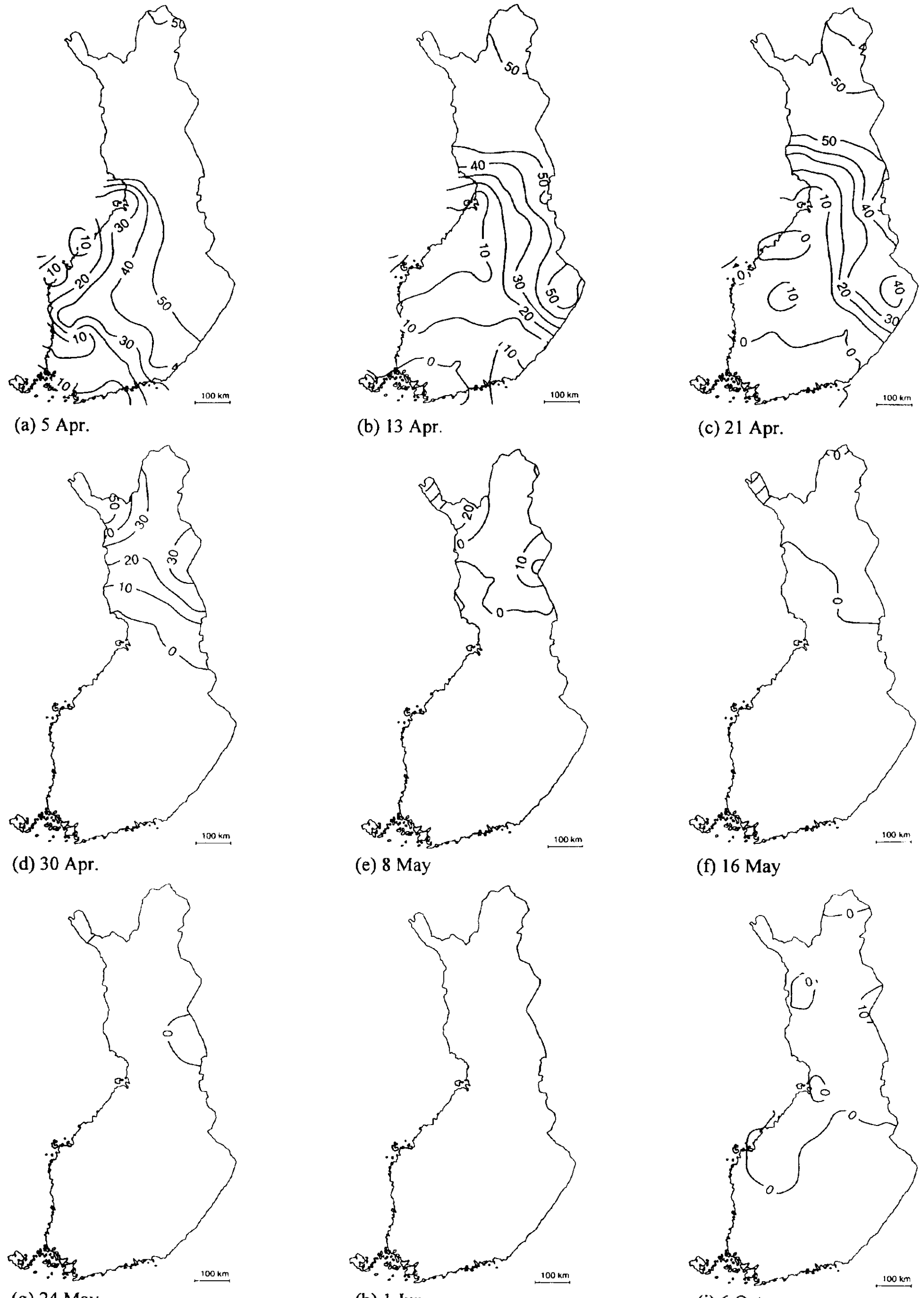


*Fig. 9.* Snow depth analyzed with linear quadratic and smoothing methods, based on station data from April to June (a–h), and in October (i) in 1994 corresponding to the albedo maps presented in Fig. 8.

albedo estimates during full snow cover conditions ranged between 20%–50% over forested terrain; only for the most northern mountainous areas, above the tree line, were regional albedos higher than 50% detected.

Estimates of regional albedos should thus strongly depend on the proportions of the main land cover types and on the presence of snow and its properties. Accurate estimates are required particularly for radiation balance calculations used, e.g., in atmospheric models.

## 5. Conclusions

Surface albedo values from averaged AVHRR images obtained with the FIMSAT satellite receiving and data acquisition system were analysed for the period from April to October in 1994 for a high latitude region. A variety of surface conditions were analysed to verify the sensitivity of the employed method to the seasonal and spatial variation in surface albedos.

In early April the highest albedo values, over 60%, occurred in the ice-covered northern part of the Gulf of Bothnia and in the northern open mountain regions. The albedo of snow-covered forested terrain in northern Finland in the subarctic zone was near 50%, contrasting with a value near 30% found typically in the middle boreal zone in eastern Finland. This difference was attributed to the higher aerial biomass density of coniferous forests in the middle boreal areas. The albedo threshold indicating the presence of snow or ice was found to be near 20%. During spring the changes in surface albedo were mainly caused by the retreating of the snow line northwards. For snow-free agricultural regions, characterised by the low spring vegetation coverage of cultivated fields, the albedo in spring was near 13% increasing to about 18% by the middle of summer, coinciding with the occurrence of maximum crop leaf cover. Overall, in the middle of summer the albedo lay in the range of 15%–18% for agricultural areas mixed with patches of forest, 11–13% for mainly forest covered terrain, 15–16% for open bogs, and was about 5% for large lakes and sea areas.

During the summer months the surface albedo obtained for agricultural areas indicated a weak but definite negative correlation with surface moisture estimated in terms of daily precipitation totals. Over forest regions this correlation was not significant.

The distributions of albedo within a few selected $24 \times 24$ pixel squares, representing different dominating surface types/terrain mosaic, were analysed for two nine-day average images selected to represent spring and mid-summer conditions, respectively. For all test squares the variation of albedo within the squares was notably greater in spring, while comparatively more stable and peaked albedo distributions were obtained in midsummer. The large spatial variation of albedo was attributed to strong contrasts in local albedos between snow-covered open and forested terrain as well as between bare soil and green coniferous forests. Over the open sea the large variation of local albedo estimates in spring was caused by the partial contributions from sea ice and open water.

The repeatability of consecutive albedo estimates depended on the accuracy of the calibration of visible and near-infrared channels, on the accuracy with which individual images could be positioned geographically, on the accuracy of the atmospheric correction and on the success in removing the cloudy pixels. To maximise repeatability, spatial averaging was performed on a grid network of $24 \times 24$ pixel squares. Temporal averaging was performed for a set of quality-controlled overpasses obtained during a nine-day period in order to average out systematic deviations due to repeating sun-target-sensor geometries.

Sensitivity analysis of the atmospheric correction algorithm showed the importance of accurately knowing the optical depth of the atmosphere. For example over snow-covered surfaces at low sun elevations, a heavy aerosol loading can cause a significant underestimation of the surface albedo if the aerosol optical depth is not known. At lower albedo levels, such as snow-free land surfaces, the influence of aerosol was shown to be less important. Overestimations can occur in the case of very small surface albedos such as water surfaces, where most of the received radiation can come from atmospheric aerosol scattering. Further improvements on monitoring of the surface variables call for methods for estimating the atmospheric aerosol optical depth from satellite data, as proposed by Laine (1992). On the basis of the sensitivity test the influence of satellite measuring geometry was considerably smaller than the influence of aerosol for estimating the surface albedo. However, the importance of solar elevation was notably significant. Even with crude average estimates of aerosol load and lacking accurate track parameters, estimates of surface albedo with the present system were realistic and comparable to those obtained by measurements from aircraft or reported in the literature for similar surface types .

## 6. Acknowledgements

We wish to express our gratitude to Mr. Eino Hellsten for his technical assistance in preparing Figs. 3 and 9, to Mr. Simo Järvenoja for making available the climatological albedos currently used in HIRLAM for comparison, and to Mr. Robin King for careful proof-reading of the manuscript.

REFERENCES

Allen, R. C. Jr., Durkee, P. and Carlyle, W. H. 1990. Snow/cloud discrimination with multispectral satellite measurements. *J. Appl. Meteor.* **29**, 994–1004.

Bringfelt B., Gustafsson N., Vilmusenaho P. and Järvenoja S. 1995. Updating of the HIRLAM physiography and climate data base. *HIRLAM Tecnical Report no. 19* (available from SMHI, Norrköping, Sweden.)

Derrien, M., Farki, B., Harang, L., LeGleau, H., Noyalet, A., Pochic, D. and Sairouni, A. 1993. Automatic cloud detection applied to NOAA-11/AVHRR Imagery. *Remote Sens. Environ.* **46**, 246–267.

Di, L. and Rundquist, D. C. 1994. A one-step algorithm for correction and calibration of AVHRR level 1b data. *Photogrammetric Engineering & Remote Sensing* **60**, 165–171.

Garand, L. 1988. Automated recognition of oceanic cloud patterns. Part I. Methodology and application to cloud climatology. *J. Clim.* **1**, 20–39.

Gerstl S. A. C. and Simmer C. 1986. Radiation physics and modelling for off-nadir satellite-sensing of non-Lambertian surfaces. *Remote Sens. Environ* **20**, 1–29.

Gutman, G. 1988. A simple method for estimating monthly mean albedo of land surfaces from AVHRR data. *J. Appl. Meteor* **27**, 973–988.

Karlsson K. G., 1989. Developement of an cloud classification model. *Int. J. Remote Sens* **10**, 687–693.

Laine, V., 1992. Atmospheric aerosol optical thickness and size distribution from satellite data over the Baltic Sea. Diss. *Commentationes Physico-Mathematicae et Chemico-Medicae* **137**, (*The Finnish Society of Sciences and Letters*).

Li, Z. and Garand, L. 1994. Estimation of surface albedo from space: A parameterization for global application. *J. Geophys. Res* **99**, 8335–8350.

Liljas, E. 1987. Automated recognition of cloudtypes from satellites and its application to nowcasting. *Int. Conf. on Agrometeorology*, Cesena 1987, Fondzione Cesena Agricultura Publ.

Paltridge, G. W. and Mitchell R. M. 1990. Atmospheric and viewing angle correction of vegetation indices and grassland fuel moisture content derived from NOAA/AVHRR. *Remote Sens. Environ.* **31**, 121–135.

Phulpin, T., Derrien, M. and Brard A., 1983. A two dimensional histogram procedure to analyze cloud cover from NOAA satellite high resolution imagery. *J. Clim. Appl. Meteorol* **22**, 1332–1345.

Solantie, R. 1988. Albedo in Finland on the basis of observations on aircraft. *Finnish Met. Institute, Meteorological Publications* **12**, 106 pp.

Saunders, R. W. and Kriebel K. T. 1988. An improved method for detecting clear sky and cloudy radiances from AVHRR data. *Int. J. Remote Sens.* **9**, 123–150.

Suttles, J. T., Green, R. N., Minnis, P., Smith, G. L., Staylor, W. F., Wielicki, B. A., Walker, I. J., Young, D. F., Taylor, V. R. and Stowe, L. L. 1988. Angular radiation models for Earth-atmosphere system, vol. 1, Shortwave radiation. *NASA Ref. Publ.* **1184**, 114 pp.

Taylor, R. V. and Stowe, L. L. 1984. Reflectance characteristics of uniform earth and cloud surfaces derived from NIMBUS-7 ERB. *J. Geophys. Res.* **89**, 4987–4996.

Teillet, P. M. and Holben B.N. 1994. Towards operational radiometric calibration of NOAA AVHRR imagery in the visible and near-infrared channels. *Canadian J. Remote Sens.* **20**, 1–10.

Van der Veen, C. J. 1992. Land ice and climate. In: *Climate System modelling*, Trenberth K. E. (ed.), p. 437–450, Cambridge University Press, 788 pp.

Wydick, J. E., Davis, P. A. and Gruber A., 1987. Estimation of broadband planetary albedo from operational narrowband satellite measurements. *NOAA Technical Report NESDIS* **27**.